Author-prepared preprint version. The official article is available at:
Damian Mendroch, Niklas Bauer, David Harings, Alexander Heisterkamp, "Deconvolution-based image enhancement for optical coherence tomography", Proc. SPIE 13006, Biomedical Spectroscopy, Microscopy, and Imaging III, 130061A (20 June 2024); https://doi.org/10.1117/12.3016987

Deconvolution-based image enhancement for optical coherence tomography

Damian Mendroch[a], Niklas Bauer[a], David Harings[a], and Alexander Heisterkamp[b]

[a]Institute for Applied Optics and Electronics, Cologne University of Applied Sciences, Betzdorfer Str. 2, 50679 Cologne, Germany.
[b]Institute for Quantum Optics, Leibniz University Hannover, Welfengarten 1, 30167 Hannover, Germany

Abstract

This work focuses on enhancing the quality of A- and B-scans of a novel linear optical coherence tomography system (LOCT), addressing the image degradation caused by noise and the blurring characteristics of the system's three-dimensional point spread function. The enhancement procedure includes an initial spatial and frequency-based pre-filtering that is applied to the measured interference pattern. Subsequently, a more robust envelope detection technique based on the Hilbert transform is employed. Lastly, image structures are reconstructed using a deconvolution algorithm based on maximum likelihood estimation, tailored to meet our unique requirements by adapting it to Rician distributed intensity values and employing a sparseness regularization term. For the deconvolution, both the lateral and axial blur of the system are considered. Emphasis is placed on the optimization of signal detection in high-noise regions, while simultaneously preventing image boundary artifacts. The efficacy of this approach is demonstrated across multiple types of measurement objects, including both artificial and biological samples. All results show a significant reduction in noise as well as enhanced resolution. Structure distinguishability is also increased, which plays a crucial role in tomography applications. In summary, the proposed enhancement method substantially improves image quality. This is achieved by still using the same initial measurement data, but incorporating prior knowledge and maximizing the amount of extracted information. Although initially designed for LOCT systems, the processing steps have potential for broader application in other types of optical coherence tomography and imaging systems.

Keywords: Optical coherence tomography, deconvolution, filtering, biomedical imaging, signal processing

1 INTRODUCTION

Optical coherence tomography (OCT) has emerged as a revolutionary imaging technique in the biomedical field, creating high-resolution cross-sectional views of living tissue. One of its most important applications is in retinal imaging, where it is used for diagnosis and monitoring of glaucoma and AMD (age-related macular degeneration). However, its use case extends well beyond the retina, with commercially available systems also scanning the eye lens or cornea, making OCT a very versatile tool in ophthalmology. Despite recent advancements, there is still an ongoing pursuit for ever-improving systems in terms of resolution, signal quality, and measurement range. Over the years, different types of these tomography systems have emerged, including swept source OCT, spectral domain OCT and time domain OCT. But at its core, each variation shares the same basic principle: Non-invasively measuring tissue through light interference in the near-infrared region.

In this technological landscape, the Cologne University of Applied Sciences is actively developing a linear optical coherence tomography (LOCT) system, a specialized offshoot of time domain OCT. The project aims to explore new approaches to OCT and provide more cost-effective solutions, especially considering the affordability for smaller medical practices. Details regarding the development of the

optical setup are documented in Bauer et al. (2024) [1]. A funduscopy system, which will be integrated at a later stage, is being developed in parallel. Harings et al. (2024) provide a description of its current state [2].

Research on signal processing techniques for LOCT is sparse, largely because its application in both research and clinical practice has been relatively limited. However, the entire field of tomography stands to benefit from a scientific endeavor aimed at narrowing the knowledge gap and exploring aspects that span across various OCT systems. Furthermore, LOCT presents a combination of broader and unique challenges, as detailed in Section 2.1: The depth signal is adversely affected by noise, low contrast, misalignment, blur, and distortion. Thus, new insights would be advantageous not only to LOCT, but also to other fields of imaging and signal processing, as many of these challenges are common across these disciplines.

The newly implemented approach aims to address these issues by enhancing the signal-to-noise ratio and contrast, thereby ensuring improved structure recognizability. Additionally, it eliminates artifacts and incorrect structures resulting from convolution, which could otherwise be mistaken for retinal layers. Clear recognizability and classification of data, especially in clinical image assessment, are indispensable, whether performed by an ophthalmologist or software

2 METHODS AND MATERIALS

2.1 Sensor Data

In LOCT, an interference pattern that contains depth information is projected onto a two-dimensional camera sensor, where the depth signal lies *linearly* along one sensor axis, with the pattern repeating on the perpendicular axis. This sensor image provides a one-dimensional scan (A-scan) at a single point on the retina. To compile area (B-scans) or volume scans (C-scans), numerous images like these must be acquired, processed and assembled. An exemplary illustration of a typical A-scan sensor image, which captures both the desired pattern and extraneous quantities, is depicted in Figure 1.

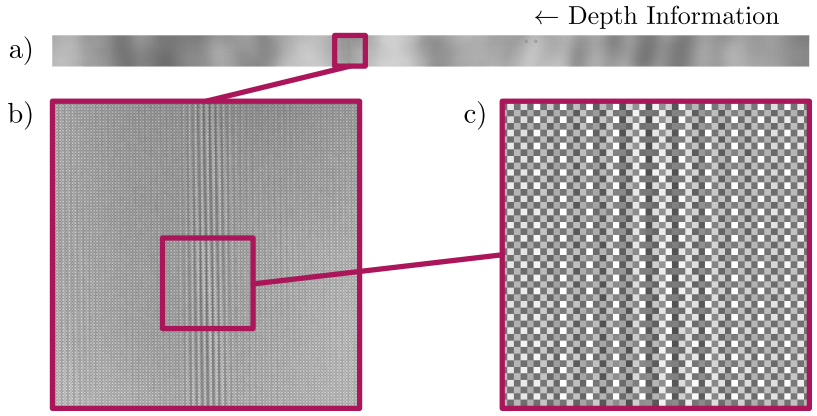

Figure 1: Exemplary camera sensor image of an A-scan. a) Multiple full sensor lines. b) Zoomed-in section with visible modulation. c) Highly magnified view revealing pixels and grid structure as a result of the Bayer pattern.

In case a), a varying base intensity across the sensor is observed. Zooming into a section of the image produces subfigure b), where the modulation pattern is now revealed. However, due to limitations in measurement and alignment, the interference pattern is slightly tilted rather than perfectly aligned. The crucial information is contained in the signal envelope, which is equivalent to the instantaneous amplitude of the modulation. Ideally, for a measurement of a sharp material boundary, one expects to see a narrow, distinct line. As shown here, this is not the case. From a physical point of view, the envelope is the result of convolving the measured object with the coherence function of the system. The coherence function, which is equivalent to the point spread function (PSF) of the system, is shaped by the source's light spectrum as well as transmission and dispersive properties of the optical setup. The convolution has the effect of blurring and introducing additional structures, particularly when the convolution kernel includes multiple peaks. View c) is the result of further magnification of the sensor image, making individual pixels visible. The observed periodic structure emerges from the interaction between the light spectrum and the

camera sensor's Bayer pattern. Variations in image intensity occur because of the different sensitivities of the three RGB pixel types to the light color. Although sensor noise is present, it is mainly concealed by the periodic structure introduced by the Bayer pattern. While a monochrome sensor would prevent the occurrence of the grid, its selection was based on other criteria, primarily the combination of pixel size and count.

Another issue arises from the low contrast of the modulation signal. Only a small range of the sensor's bit depth is utilized, leading to relatively larger quantization errors and therefore less accuracy. Weaker signals are discretized even less accurately or are not detectable at all. Interestingly enough, the acquisition benefits from the disturbances inside the image: In combination with the redundancy of the pattern, an increase in sensor bit depth can be achieved. This phenomenon is caused by the noise acting as a probabilistic dither, which leads to the values being digitized differently in every sensor line. When averaged over a larger scale, the noise is filtered and an image region with values seemingly in-between bit levels is created. Such sub-bit resolution enhancement is found in other fields of signal processing, for instance in dithering in analog-to-digital converters (ADCs), as described in a whitepaper by National Instruments [3]. An increased bit depth also enables the detection of smaller signal components, however, it cannot be utilized as long as noise and other polluting signals are still present.

2.2 Processing Overview

Generating a high-quality OCT scan, despite all these challenges, requires a customized processing strategy. This study extends the foundational work presented by Bauer et al. (2024) [1], as visually summarized on the left side of Figure 2. While the processing yields results that are functional to a degree, it does not resolve certain issues. Notably, the approach does not address the blurring and emergence of incorrect structures that result from the convolution. There is room for improvement in the filtering technique as well, as it does not reduce the noise to the fullest possible extent. Additionally, severe boundary artifacts arise from the combination of absent padding and a suboptimal rectangular window in the Fourier domain.

The improved approach aims to address these problems and is listed on the right side of Figure 2. Subsequent sections provide further elaboration on these techniques and their implementation.

Bauer et al. (2024) [1]

1. Fourier-domain based bandpass filtering and removal of negative frequencies
2. Inverse Fourier transform
3. Magnitude calculation on the resulting complex image
4. Spatial averaging over a few lines
5. Joining A-scans to a B-scan
6. Image adjustments (brightness, contrast, false color)

Improved Approach

1. Rotation detection by the Radon transform
2. Spatial averaging along the redundant axis
3. Bandpass filtering
4. Envelope detection by conversion to an analytical signal
5. Joining A-scans to a B-scan
6. Iterative deconvolution
7. Image adjustments (brightness, contrast, false color)

Figure 2: Comparison of the previous and new processing framework.

2.3 Image Padding

Image rotation, filtering, deconvolution, and envelope detection are all susceptible to boundary effects. These effects arise from erroneous assumptions about outside data, like assuming zero values, or from intrinsically imposing certain boundary conditions, such as continuity between opposite edges. To mitigate these issues, the processing strategy employs a reflection padding prior to each step, which mirrors the data around each edge of the image. As a result, discontinuities at the original boundaries are eliminated. Notably, this approach also preserves statistical properties, as value range and frequency distribution are

transferred in to the new areas. After completing the steps susceptible to boundary effects, the padded regions are removed. Although edge artifacts still occur at the new boundaries, their impact is now outside the region of interest. Within the improved framework, reflection padding is systematically applied to the techniques in Sections 2.4 to 2.8.

2.4 Spatial Averaging

The orientation of the interference pattern is detected by using the Radon transform, a technique that mirrors the methodology used by Silva et al. (2021) [4]. In essence, this approach identifies the angle at which the pattern is projected with minimal distortion and most sharply onto a fixed axis. After determining the angle, the image is averaged in the perpendicular axis. This strategy produces a one-dimensional depth signal with considerably reduced noise.

2.5 Bandpass Filtering

The signal components under investigation lie in a fixed frequency range, centered around the modulation frequency. Frequencies outside this range are composed of noise and undesired signals with no relevant information, including the base intensity of the image or the Bayer pattern. Consequently, employing a frequency-selective filter to eliminate these extraneous components is justified.

Schmid et al. (2022) present a modified sinc filter kernel that balances noise suppression and oscillatory artifacts [5]. The kernel, consisting of a sinc-function with a special window function, is designed to balance stopband attenuation, passband flatness, ringing, and overshoot. In its original formulation, the kernel acts as a low-pass filter. To achieve high-pass filtering, the difference between low-pass filtered signal and initial counterpart has to be computed. However, for our purposes, a bandpass filter is required. To accomplish this, the shift theorem of the Fourier transform is employed: Modulating the kernel in the original domain, correspondingly shifts the signal in frequency domain by exactly the modulation frequency.

2.6 Envelope Detection

Gianto et al. (2016) explore a variety of envelope detection methods for OCT [6]. The authors conclude that both the wavelet transform and Hilbert transform yield superior results. While the wavelet transform is recognized for its enhanced filtering capabilities, it is also noted that such filtering introduces minor distortions to the signal. Given that the framework performs the filtering process independently, the Hilbert transform approach proves sufficient for envelope detection. With the help of this transformation the image is converted into a analytic signal, where the data now consist of complex numbers. Here, the envelope, synonymous with the instantaneous amplitude, is contained as the complex magnitude, while the instantaneous phase is reflected in the complex argument.

2.7 Noise Characterization

Probabilistic estimation methods rely on the knowledge of the noise distribution and its parameters. The conversion of the modulated signal to an analytic signal generates a rotating vector in the complex plane. When the modulation signal is superimposed with Gaussian noise, both the real and imaginary parts of the vector are Gaussian distributed. For such a symmetrical, non-central, two-dimensional Gaussian function, the distance to the origin is Rician distributed [7]. In the context of an analytic signal, the radial distance equates to the magnitude of the complex number, and by extension to the signal envelope under investigation. Equivalent phenomena arise in MRI (magnetic resonance imaging) applications as well as in specific scenarios in multipath propagation [8, 7].

The probability density function f of a Rician distributed variable $R(\nu, \sigma)$ is given as [7]:

$$f\left(r \,|\, \nu,\, \sigma\right) = \frac{r}{\sigma^2} \exp\left(-\frac{r^2+\nu^2}{2\sigma^2}\right) I_0\left(\frac{r\nu}{\sigma^2}\right) \tag{1}$$

Here, I_0 denotes the modified bessel function of the first kind with order zero and σ describes the standard deviation. ν represents the true, undisturbed value, while r is the distribution variable. Examples of multiple functions are displayed in Figure 3.

The density function transforms into a Rayleigh distribution, when $\nu = 0$, while for $\nu \gg \sigma$ it approaches a Gaussian distribution. Thus, not only does its density function evolve with changes in relative

signal strength, but its symmetry does as well. As a further complication, the envelope detection rectifies noise and assigns it to the instantaneous amplitude. This results in a shift between the expectancy value of the distribution and the true value ν, a phenomenon referred to as *Rician bias*. The bias varies according to the signal strength relative to the noise floor, therefore particularly affecting regions with low signal-to-noise ratio.

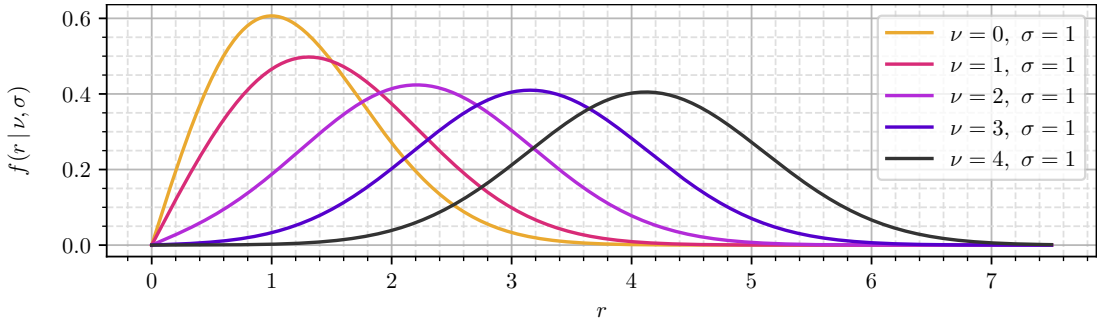

Figure 3: Probability density function f of a Rician distribution for a fixed $\sigma = 1$ and varying ν.

The accurate determination of σ from arbitrary image locations poses a significant challenge due to these characteristics. Instead, the characterization is limited to regions with Rayleigh distributed data. The literature reveals various relationships between σ and other metrics of the Rayleigh distribution. Among others, they include the mean, median, mode and variance [9, 10]. Additionally, the maximum likelihood estimation provides a viable pathway for a best guess of σ [11]. In this work, the implemented framework reliably estimates the standard deviation using the median of dark image regions. Let b be a measured image, where each value b_i is a sample of a Rician distributed variable $R(\nu_i, \sigma)$. Then $b_{\nu=0} \subset b$ represents a pixel set from locations, which are expected to be devoid of any signal. For a sufficiently large number of values in $b_{\nu=0}$ the following approximation holds:

$$\sigma \approx \frac{1}{\sqrt{\ln 4}} \operatorname{median}(b_{\nu=0}) \tag{2}$$

The rationale behind employing a median-based method resides in its inherent resilience to outliers, which may manifest as salt-and-pepper noise, areas of missing data, or zones erroneously classified as signal-absent.

2.8 Deconvolution

2.8.1 Base Algorithm

Verveer et al. (1999) and Pantin et al. (2001) reviewed several methods available for deconvolution [12, 13]. For the data under investigation, a maximum likelihood estimation (MLE) strategy was chosen. Essentially, MLE not only reverse convolution, but in the process also separates the image into signal and noise components, while accounting for both the amplitude and frequency distribution of the noise.

Canales-Rodríguez et al. (2015) introduced a MLE-based deconvolution algorithm for Rician distributed data, the Robust and Unbiased Model-BAsed Spherical Deconvolution (RUMBA-SD) [14]. Given an image vector b, a blur matrix A, the standard deviation σ of the noise, the deconvolved image vector x in the k-th iteration is defined as follows: [1]

$$x_{k+1} = x_k \circ \frac{A^T \left(b \circ \frac{I_1\left(\frac{b \circ (Ax_k)}{\sigma^2}\right)}{I_0\left(\frac{b \circ (Ax_k)}{\sigma^2}\right)} \right)}{A^T A x_k + \epsilon} \tag{3}$$

In Equation 3, I_0 and I_1 represent the modified Bessel function of the first kind, of orders zero and one, respectively. The superscript ^{T} indicates the transpose operator and $\circ$ symbolizes the Hadamard product, which is the element-wise multiplication of two vectors. The division in this expression is also executed on an element-wise basis. A small, positive value $\epsilon > 0$ is added to the denominator to avoid divisions by zero. Starting with an initial x_0, which is filled with ones, the algorithm iteratively refines and optimizes the result, step by step. The multiplicative formulation of the algorithm guarantees the

[1] In fact, RUMBA-SD also includes a MLE for an unknown σ in each iteration, in contrast to our approach, which applies a fixed value for σ.

positivity of the output x_k, as long as all components of b, A and x_0 are positive. Positivity is an important requirement in OCT, as the data represent intensity values. Although RUMBA-SD performs the deconvolution directly, it also easily derives the denoised measurement: Referring back to Equation 1, each element of the re-convolved image $(Ax_k)_i$ estimates the undisturbed value ν_i for measurement b_i.

With the assumption of a spatially invariant kernel, Ax_k simplifies to a convolution term $x_k \circledast a$, whereas $A^T x_k$ translates to $x_k \circledast a^*$. In these expressions, a denotes a kernel vector and a^* represents its 180° degree rotated version. With these adaptions the algorithm becomes:

$$x_{k+1} = x_k \circ \frac{\left(b \circ \frac{I_1\left(\frac{b(x_k \circledast a)}{\sigma^2}\right)}{I_0\left(\frac{b(x_k \circledast a)}{\sigma^2}\right)} \right) \circledast a^*}{(x_k \circledast a) \circledast a^* + \epsilon} \tag{4}$$

2.8.2 Regularization

One inherent challenge with MLE-based methods is the phenomenon of divergence beyond a certain number of iterations. This effect results from noise amplification and overinterpretation of minor image differences [15, 16]. Furthermore, the solution space is exceedingly large because the estimation attempts to reconstruct signal components obscured by noise, lost in the blur or absent in the numerical precision of the data. Regularization offers a viable strategy to address these issues and steer the deconvolution towards the desired solution.

In our case, applying common regularization methods, such as total variation, is deemed unnecessary because our deconvolution process does not advance to the point of divergence. Instead, sparseness regularization is favored, a technique designed to eliminate abundant image elements, particularly targeting the reduction of faint and spot-like features. The technique introduced by Shaked et al. (2011) [17] results in an efficient implementation by adding a small positive offset $\lambda_{\text{sp}} > 0$ into the denominator of the Richardson-Lucy iteration. Following the same procedure, an equivalent expression for Rician data is obtained:

$$x_{k+1} = \Psi\left(x_k\right) = x_k \circ \frac{\left(b \circ \frac{I_1\left(\frac{b(x_k \circledast a)}{\sigma^2}\right)}{I_0\left(\frac{b(x_k \circledast a)}{\sigma^2}\right)} \right) \circledast a^*}{(x_k \circledast a) \circledast a^* + \epsilon + \lambda_{\text{sp}}} \tag{5}$$

In subsequent sections, the symbol Ψ is used to represent the convolution iteration. For readers interested in equivalent MLE formulations for Poisson or Gaussian noise, detailed explanations are available in appendix A.

2.8.3 Acceleration

The current implementation requires a considerable amount of iterations to yield acceptable results, typically in the higher double digits. Algorithmic acceleration is desirable, considering that each iteration involves multiple convolutions, operations significantly more complex than basic arithmetic such as addition or multiplication.

A first optimization involves reusing the result of $x_k \circledast a$ in Equation 5, thereby reducing the number of convolutions per iteration from five to three. Furthermore, Biggs and Andrews (1997) introduced a promising approach to reduce the number of required iterations [16]. Instead of utilizing the preceding result x_k, the method incorporates an extrapolated term y_k into the deconvolution iteration:

$$x_{k+1} = \Psi\left(y_k\right) \tag{6}$$

Here, y_k is defined as follows:

$$y_k = x_k + \alpha_k \left(x_k - x_{k-1}\right) \tag{7}$$

In Equation 7, x_k is linearly extended by leveraging the difference in images between the last iterations. This extension is moderated by a scaling factor α_k, referred to as *acceleration factor*, calculated as follows:

$$\alpha_k = \frac{\sum g_{k-1} \cdot g_{k-2}}{\sum g_{k-2} \cdot g_{k-2}}, \quad 0 \leq \alpha_k \leq 1 \tag{8}$$

Here g_{k-1} and g_{k-2} are defined as:

$$\begin{aligned} g_{k-1} &= x_k - y_{k-1} \\ g_{k-2} &= x_{k-1} - y_{k-2} \end{aligned} \tag{9}$$

Put differently, g_k characterizes the vector of change between iterations when viewed within a geometrical context. The term $\sum g_{k-1} \cdot g_{k-2}$ is equivalent to a scalar product of difference vectors of the last two iterations. Its value tends to be smaller when changes occurred in different locations, with the vectors being orthogonal in the most extreme case, and larger when the vectors are similar or even parallel. The acceleration factor is normalized using the sum of squares of g_{k-2}, establishing a relative metric for extrapolation. Moreover, confining the value of α_k within the range $[0, 1]$ is critical to maintain the stability of the acceleration.

This approach, referred to as *automatic acceleration*, dynamically adjusts the degree of extrapolation based on the effectiveness in the recent iterations. A straightforward analogy is the strategy of a race car driver who accelerates on straight stretches where the road's direction aligns with the vehicle's motion vector but slows down in curves to effectively adjust the trajectory.

In practical terms, implementing this strategy has resulted in a reduction of the number of iterations by a factor of eight. Consequently, the acceleration lowered the processing time by the same factor, while simultaneously producing comparable results.

2.8.4 Kernel Determination

Since the convolution kernel corresponds to the PSF, it can be empirically derived as the system's impulse response. In the axial direction, the kernel can be ascertained through the examination of a thin object layer or a highly reflective boundary, such as a mirror. Within our setup, the resulting shape features a distinct peak, flanked by sides that gradually diminish, each side containing multiple secondary maxima. We direct readers to the work of Bauer et al. (2024) for a presentation of the axial profile curve [1]. This methodology is similarly applied to the lateral dimension, yielding a profile that closely resembles a Gaussian function. It is critical for subsequent processing steps to ensure the kernel is normalized, maintaining a cumulative sum of one. The normalization ensures that the integral power is preserved and the deconvolved image retains its true intensity values.

2.8.5 Stopping Criterion

Conventionally, the algorithm is terminated once the changes between subsequent iterations fall below a specified threshold, indicative of reached convergence. In contrast, our method terminates the process preemptively, set by a predefined number of iterations. This decision rests on three considerations: First, limiting iterations decreases processing time. Second, fully deconvolved images can appear unnatural, characterized by unrealistically thin and sharp structures. Third, the algorithm holds a risk of misinterpreting specific image elements. Artifacts, inaccuracies in the convolution kernel, or signal distortions may be overinterpreted, resulting in incorrect outcomes. By halting the algorithm earlier on, the perceptual naturalness of the images is retained.

2.9 Image Adjustments

Even now, the results remain impractical for medical evaluation: As the processed data is still linear to the object's backscattering properties, the image contains a wide range of intensities. This is due to tissue having boundaries with different changes in refractive index and regions differing in absorptance levels. Consequently, a non-linear value mapping is desirable to visualize as many structural details as possible. The non-linear brightness perception of the human eye represents a promising candidate for such mapping. Its function is approximated by the lightness channel of the CIELUV 1976 color space, as defined by the ISO 11664 standard [18]. In our implementation, the conversion is aided by slight brightness and contrast adjustments to further enhance visibility. To augment visual appeal and clarity, images are rendered in false colors. This technique not only enriches their aesthetic value, but also introduces a color contrast to improve the distinction between light and dark areas.

3 RESULTS

Figure 4 illustrates the stepwise improvements obtained from applying different processing procedures to a B-scan of an adhesive tape stack. The first image demonstrates the outcome of the methodology proposed by Bauer et al. (2014) [1]. Noise is prominently visible in this result. Although individual layers are distinguishable, the presentation lacks uniformity. Subsequent results will reveal that a portion of the observed elements are in fact no actual structures in the tape stack, but a result of the convolution. The

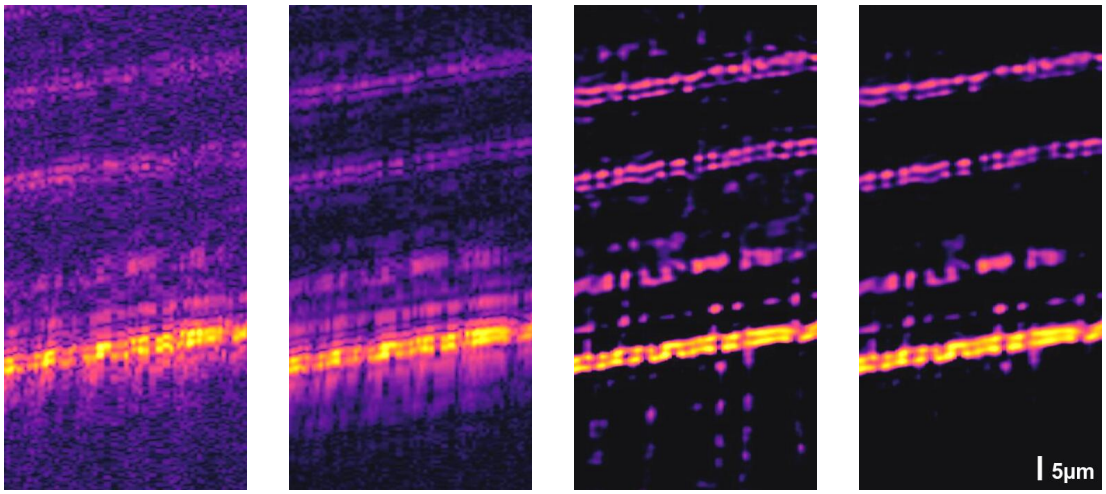

Figure 4: From left to right: 1) Previous approach from Bauer et al. (2024) [1]. 2) New approach, but without the deconvolution step. 3) New approach with deconvolution, but without sparseness regularization, $k = 10$, $\lambda_{\text{sp}} = 0$. 4) New approach with deconvolution and sparseness regularization, $k = 10$, $\lambda_{\text{sp}} = 2.4\sigma$.

second image presents our new method, albeit omitting the deconvolution step. A noticeable reduction in noise is evident, alongside a greater uniformity in layer structure. In the third image, the deconvolution procedure is now included, excluding only the sparseness regularization that has been deactivated by setting $\lambda_{\text{sp}} = 0$. There is an improved clarity, especially around the lowest layer. This suggests that the deconvolution process effectively "cleans up" the surroundings, eliminating elements not corresponding to genuine physical structures. The effect on the upper layers is less pronounced, as parts of the PSF are concealed by the background noise. The image clarity is significantly enhanced with the application of sparseness regularization, as evidenced in the fourth image. The regularization technique leads to the elimination of isolated spots across the image. The change is particularly evident in areas between layers where, theoretically, no meaningful data should be present.

In fact, the previous images show a more intricate situation for demonstration purposes: The layers in Figure 4 originate from a deeper measurement depth within the object also measured in Figure 5. Due to a larger path through a dispersive medium, a disparity between the assumed and actual coherence function arises. The mismatch manifests itself as the presence of remaining isolated points that can be observed around the lowest layer in the third subfigure. While the regularization in the fourth subfigure erases most of the structures below the layer, unfortunately, most spots above the layer remain.

Figures 5 through 8 illustrate results of larger scale data. Specifically, Figure 5 demonstrates the application of the processing technique to a stack of adhesive tape. There is a significant contrast enhancement and an increase in structural clarity, which highlights the effectiveness of our approach. Additionally, boundary artifacts are noticeable in the processing from Bauer et al. (2024) around the top of the image. By implementing reflective padding within the processing steps, these boundary effects are successfully prevented.

Figure 6 displays optically printed diffraction gratings with varying height. In this side view, grating bars are aligned perpendicular to the image plane, whereas the grating gaps would be discernible horizontally. However, due to the limited lateral resolution of our OCT system, they are not visible in the measurement. When comparing both outcomes, the new processing results in a large decrease in noise and a clearer separation of the gratings against the background. As surrounding structures are discarded, the height of the bars, visible as a gap between upper and lower layer, is now easier to differentiate. Effectively, resolution is increased, which is especially noticeable in the first two gratings.

Figures 7 and 8 provide insight into the imaging of biological specimens, showcasing scans of two types of grapes. Consistent with observations made in other images, these figures demonstrate improved contrast and enhanced structural details. A notable difference in these results, as compared to earlier non-biological samples, is the presence of speckles. These speckles are granular patterns that arise due to the interference created by the scattering of light within the medium, as it encounters various particles or inhomogeneities. Such patterns were absent for technical samples, which typically consist of clearer media and are characterized by well-defined material boundaries. The occurrence of speckling presents a current challenge to our OCT setup when imaging tissue and other biological samples. It is important

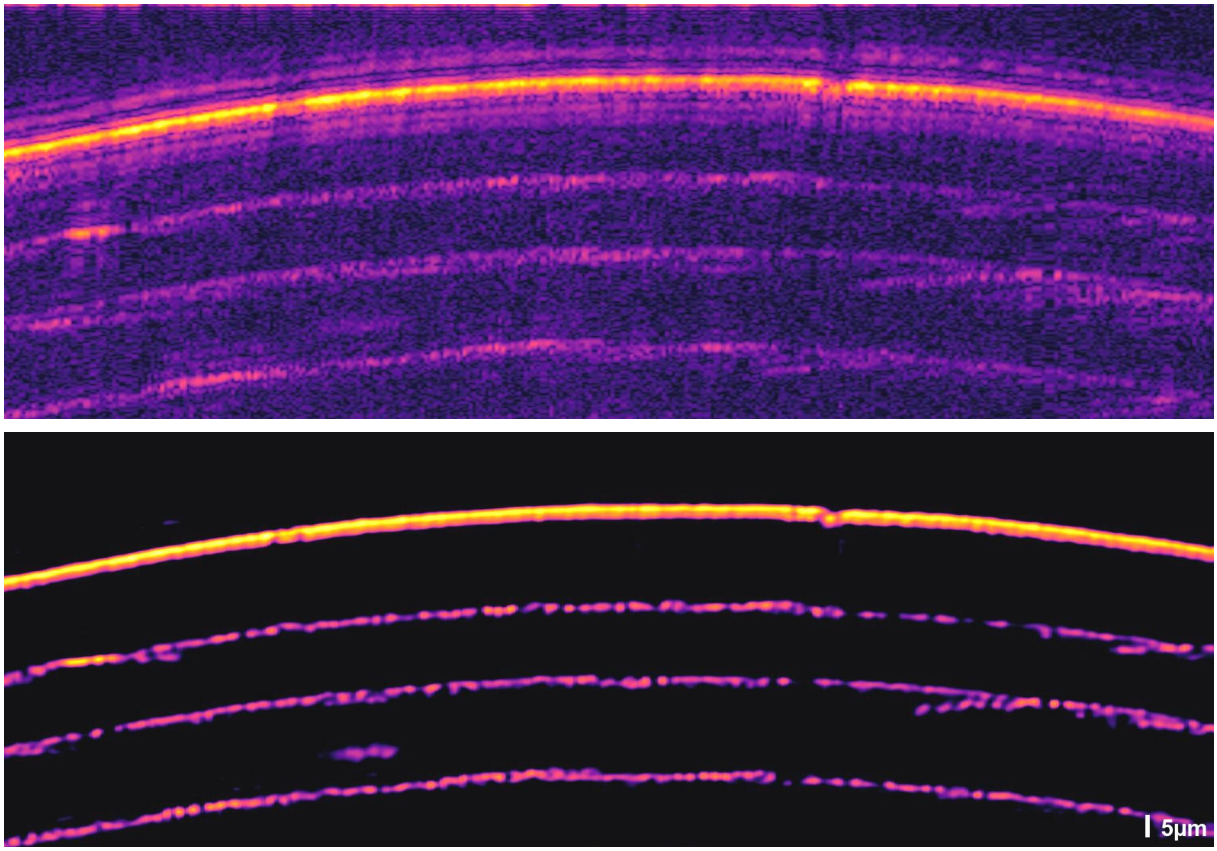

Figure 5: B-scan of a adhesive tape stack. The top image shows the previous approach, the bottom one the improved approach. The deconvolution parameters are $k = 10,\ \lambda_{\mathrm{sp}} = 1.6\sigma$.

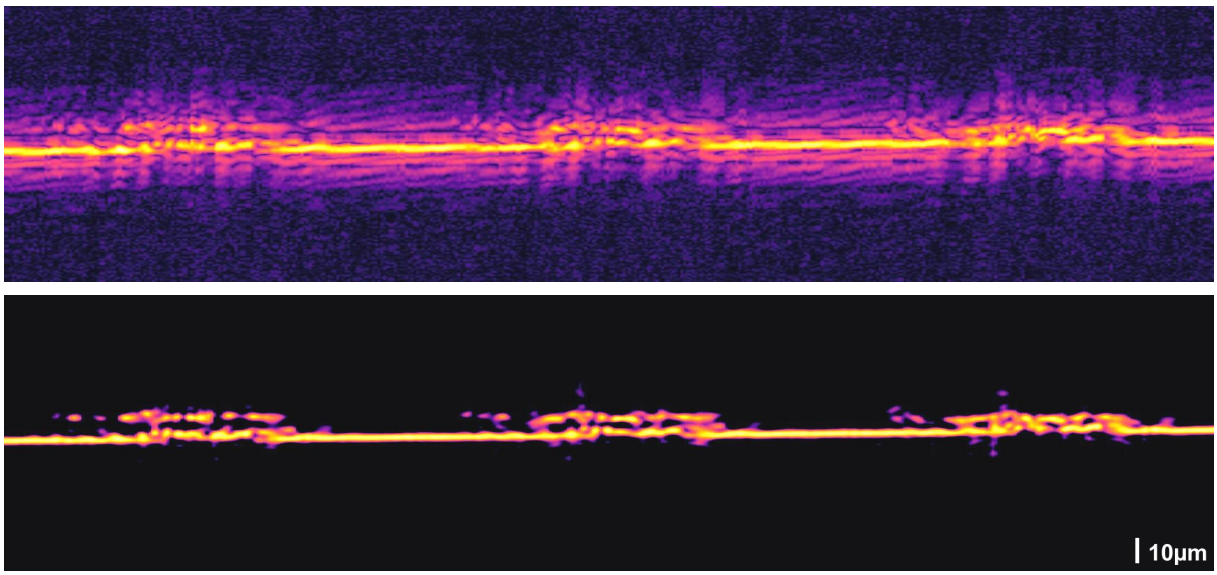

Figure 6: B-scan of optically printed diffraction gratings. The grating heights equal 8 µm, 6 µm and 4 µm. The top image shows the old approach, the bottom one the new approach with parameters $k = 10,\ \lambda_{\mathrm{sp}} = 8\sigma$.

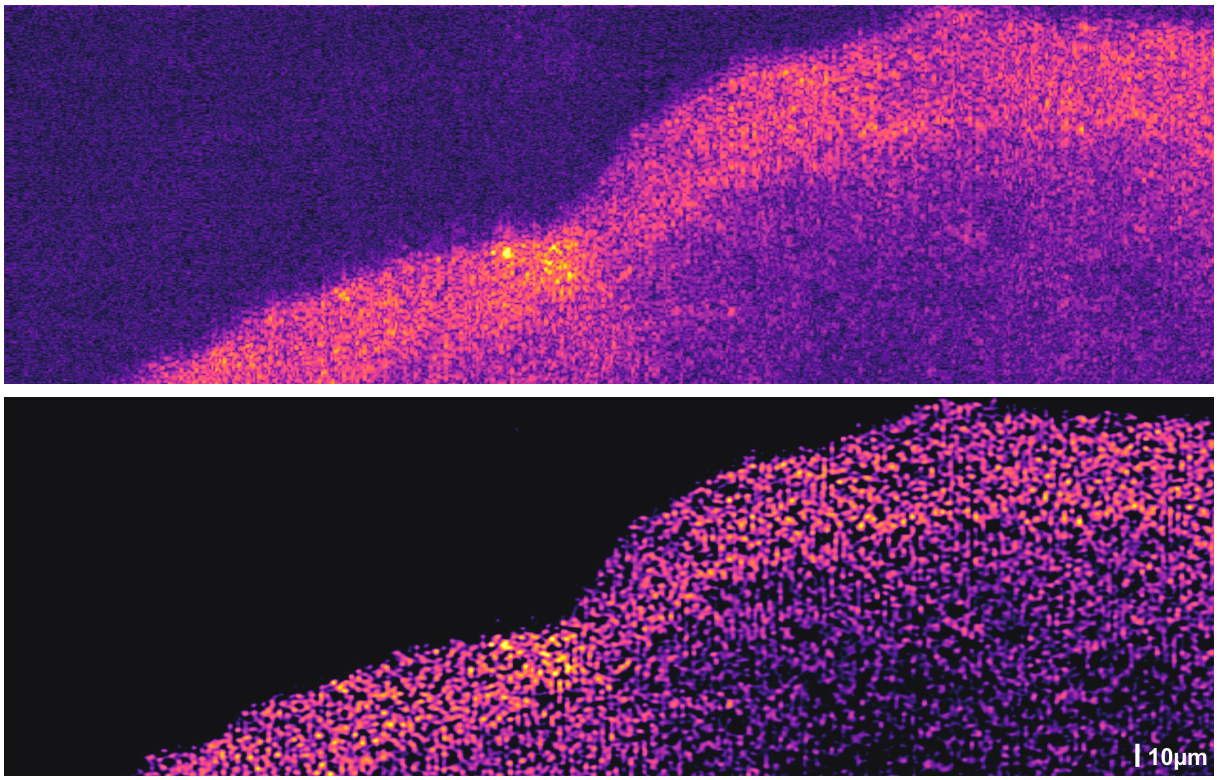

Figure 7: B-scan of a grape. The top image shows the old approach, the bottom one the new approach with parameters $k = 10,\ \lambda_{\text{sp}} = 2.4\sigma$.

to note that the presence is not linked to the processing, but related to the imaging capabilities of the system. Addressing these issues is crucial for future enhancements to the system.

4 DISCUSSION

The results demonstrate a significant enhancement in the quality of the images. Specifically, the elimination of the Rician bias noticeably improves the contrast of the data. This enhancement is attributed to the combined effects of advanced filtering techniques and deconvolution by likelihood maximization, which together reduce noise levels and yield a dark background. Furthermore, such processing results in images with markedly sharper structures, characterized by clear and well-defined boundaries. Additionally, artifacts that were introduced by the convolution and mimicking structural features are now accurately identified and eliminated. The improvement is particularly evident in the examples showcased in Figures 5 and 6. In the field of medical imaging, the depiction of layer positions and thicknesses is critical for the accurate diagnosis and classification of pathological conditions. Therefore, the ability to detect these features with high precision and clarity is indispensable. Enhancements, such as additional contrast adjustments and color mapping, further amplify the visibility of crucial details. An increased resolution is particularly evident in the data of Figure 6. These achievements align perfectly with the objectives specified in the introduction, demonstrating the efficacy of our approach. It is important to note that these outcomes were achieved by harnessing prior knowledge, which encompasses the interference pattern's redundancy, the characteristics of noise, the signal's frequency range, the coherence function of the system, and the anticipated properties of the specimens. The strategic incorporation of this knowledge into our methodology maximizes the quality of the data extracted.

The impact of the regularization is best demonstrated in Figure 4, showcasing the effective removal of point-like structures. The dimensioning of the sparseness regularization, controlled by the number of iterations and the regularization parameter, varies based on the statistical characteristics of the image. More specifically, the choice of parameters is linked to the signal and noise properties in the measurements: In scenarios where the image is populated with numerous spot-like features, discerning between genuine data and noise becomes challenging. Conversely, in measurements with distinct, extensive structures, spots are more likely to represent noise, allowing for an increase in the sparseness parameter. The parameter selection ultimately hinges on the trade-off between detail preservation and noise reduction one

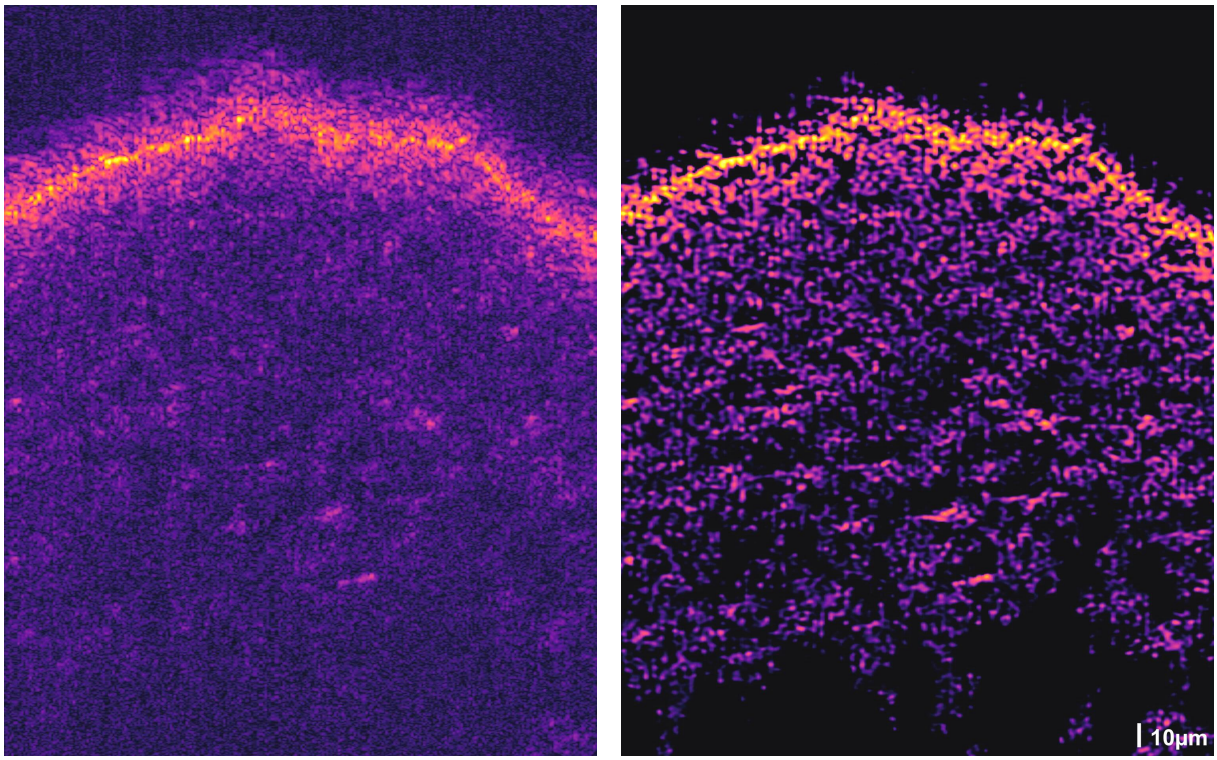

Figure 8: B-scan of a second type of grape. The left image shows the old approach, while the right one the new approach with parameters $k = 10,\ \lambda_{\text{sp}} = 1.2\sigma$.

is prepared to accept. Discrepancies in the sparseness parameter settings across our figures are a reflection of an empirical choice. Moreover, the purpose of the sparseness regularization extends beyond addressing noise-induced outliers. As presented in the result section, it also partly corrects subtle discrepancies in the convolution kernel.

Unfortunately, the process is not without its limitations. The deconvolution fails to correctly map values onto the PSF when there are excessive differences in the kernel. This leads to persistent, remaining structures without a base in reality. To mitigate this issue, an additional step should be included that compensates for the dispersion and absorption in different imaging depths. Alternatively, future modifications could allow for the use of a depth-dependent convolution kernel. Another limitation is the erroneous removal of correct structures. This issue is twofold, where one factor is the chosen degree of sparseness regularization and the other is rooted in the nature of the data: Particularly in situations where the signal-to-noise ratio is diminished, certain intensity values are not significant enough to be accurately identified. Despite the incorporation of probabilistic assessments, the solutions derived are estimations, representing a "best guess" that may not align with the true nature of the measured object.

In summary, the efficacy of the presented image enhancement technique has been proven, offering significant improvements in quality, contrast and clarity. These properties have been demonstrated on both artificial and biological samples, thereby demonstrating applicability for a variety of use cases. Due to its modular nature, adaptability is ensured as well, consequently making it suitable for a broader range of applications, including other types of OCT systems and imaging technologies.

A REGULARIZED MLE FOR GAUSSIAN AND POISSON NOISE

The noise distribution within an image significantly influences the selection of an appropriate MLE deconvolution algorithm. Typically, these algorithms operate under the assumption of spatially uncorrelated noise, which is commonly referred to as white noise. However, they differ in terms of amplitude distribution.

The predominant form of noise encountered in photographic images is Poisson distributed. A prominent method tailored to this type of noise is the Richardson-Lucy algorithm [19, 20]. Equation 10 provides a sparseness regularized MLE iteration, similar to Equation 5, as modification of this algorithm. To pro-

duce correct results, it is imperative that the kernels a and a^* undergo normalization, so their integral values amount to one.

$$x_{k+1} = x_k \circ \left(\frac{b}{x_k \circledast a + \epsilon} \circledast a^* \right) \circ \frac{1}{1 + \lambda_{\text{sp}}} \tag{10}$$

When intensity values significantly exceed the variations attributed to noise, applying the central limit theorem becomes feasible. Under these conditions, the Poisson distribution is effectively approximated by a Gaussian distribution. For this noise characteristic, a well-known iterative deconvolution algorithm is ISRA (Image Space Reconstruction Algorithm) [21]. An adapted, regularized version of ISRA is then:

$$x_{k+1} = x_k \circ \frac{b \circledast a^*}{x_k \circledast (a \circledast a^*) + \epsilon + \lambda_{\text{sp}}} \tag{11}$$

A notable benefit of Equation 11 lies in its computational efficiency, which is achieved through the strategic reuse of both $b \circledast a^*$ and $a \circledast a^*$. Since these components are invariant across iterations, each iteration can be simplified to contain just a single convolution operation. Compared to the algorithm adapted to Poisson noise, this optimization halves the computational burden associated with the convolution.

Both algorithms operate iteratively, assume a locally independent kernel and guarantee a positive solution for x_k, similar to RUMBA-SD in Section 2.8. Given that Equations 10 and 11 only provide the deconvolution iteration term $\Psi(x_k)$, all other procedural enhancements remain unaffected. Specifically, strategies related to padding and acceleration, as detailed in Sections 2.3 and 2.8.3, retain their applicability and can be seamlessly integrated. By design, the presented approach maintains a high degree of flexibility, allowing for further optimization in accordance with the specific requirements of the deconvolution task at hand.

ACKNOWLEDGMENTS

This research received funding from the German Federal Ministry of Education and Research (German: Bundesministerium für Bildung und Forschung - BMBF), under funding reference number 13FH141KX1.

References

[1] N. Bauer, D. Mendroch, D. Harings, J. Matrisch, U. Oberheide, and A. Heisterkamp, "Development of a linear optical coherence tomography low-cost system for ophthalmic applications," in *Biomedical Spectroscopy, Microscopy and Imaging III*, SPIE, Apr. 2024.

[2] D. Harings, N. Bauer, D. Mendroch, D. Harings, U. Oberheide, and H. Lubatschowski, "Real-time video funduscopy with continuously moving fixation target," in *Biomedical Spectroscopy, Microscopy and Imaging III*, SPIE, Apr. 2024.

[3] National Instruments, "Analog sampling basics." https://web.archive.org/web/20150926163457/http://www.ni.com/white-paper/3016/en/pdf, 2014. [Accessed 12.03.2024].

[4] R. R. d. Silva, M. C. Escarpinati, and A. R. Backes, "Sugarcane crop line detection from UAV images using genetic algorithm and radon transform," *Signal, Image and Video Processing*, vol. 15, pp. 1723–1730, Apr. 2021.

[5] M. Schmid, D. Rath, and U. Diebold, "Why and how Savitzky–Golay filters should be replaced," *ACS Measurement Science Au*, vol. 2, pp. 185–196, Feb. 2022.

[6] G. Gianto, F. Salzenstein, and P. Montgomery, "Comparison of envelope detection techniques in coherence scanning interferometry," *Applied Optics*, vol. 55, pp. 6763–6774, Aug. 2016.

[7] A. Papoulis and S. U. Pillai, *Probability, Random Variables and Stochastic Processes*. McGraw-Hill, 4 ed., 2002.

[8] A. Cárdenas-Blanco, C. Tejos, P. Irarrazaval, and I. Cameron, "Noise in magnitude magnetic resonance images," *Concepts in Magnetic Resonance Part A*, vol. 32A, pp. 409–416, Nov. 2008.

[9] D. A. Abraham, *Mathematical Statistics*, p. 251–305. Springer International Publishing, 2019.

[10] S. Aja-Fernandez, C. Alberola-Lopez, and C.-F. Westin, "Noise and signal estimation in magnitude MRI and rician distributed images: A LMMSE approach," *IEEE Transactions on Image Processing*, vol. 17, p. 1383–1398, Aug. 2008.

[11] J. Sijbers, A. den Dekker, D. Dyck, and E. Raman, "Estimation of signal and noise from Rician distributed data," in *Proceedings of International Conferences on Signal Processing and Communications*, (Las Palmas de Gran Canaria, Spain), pp. 140–143, Feb. 1998.

[12] P. J. Verveer, M. J. Gemkow, and T. M. Jovin, "A comparison of image restoration approaches applied to three-dimensional confocal and wide-field fluorescence microscopy," *Journal of Microscopy*, vol. 193, pp. 50–61, Jan. 1999.

[13] E. Pantin, J.-L. Starck, and F. Murtagh, *Deconvolution and Blind Deconvolution in Astronomy*, ch. 1, pp. 1–38. CRC Press, 2001.

[14] E. J. Canales-Rodríguez, A. Daducci, S. N. Sotiropoulos, E. Caruyer, S. Aja-Fernández, J. Radua, J. M. Y. Mendizabal, Y. Iturria-Medina, L. Melie-García, Y. Alemán-Gómez, J.-P. Thiran, S. Sarró, E. Pomarol-Clotet, and R. Salvador, "Spherical deconvolution of multichannel diffusion MRI data with non-gaussian noise models and spatial regularization," *PLOS ONE*, vol. 10, p. e0138910, Oct. 2015.

[15] R. L. White, "Image restoration using the damped Richardson-Lucy method," in *Instrumentation in Astronomy VIII* (D. L. Crawford and E. R. Craine, eds.), pp. 1342–1348, SPIE, June 1994.

[16] D. S. C. Biggs and M. Andrews, "Acceleration of iterative image restoration algorithms," *Applied Optics*, vol. 36, pp. 1766–1775, Mar. 1997.

[17] E. Shaked, S. Dolui, and O. V. Michailovich, "Regularized Richardson-Lucy algorithm for reconstruction of Poissonian medical images," in *2011 IEEE International Symposium on Biomedical Imaging: From Nano to Macro*, IEEE, Mar. 2011.

[18] International Standard Organization, "ISO/CIE 11664-5:2016 - Colorimetry Part 5: CIE 1976 L*u*v* colour space and u', v' uniform chromaticity scale diagram," 2016.

[19] W. H. Richardson, "Bayesian-based iterative method of image restoration," *Journal of the Optical Society of America*, vol. 62, pp. 55–59, Jan. 1972.

[20] L. B. Lucy, "An iterative technique for the rectification of observed distributions," *The Astronomical Journal*, vol. 79, pp. 745–754, June 1974.

[21] M. E. Daube-Witherspoon and G. Muehllehner, "An iterative image space reconstruction algorithm suitable for volume ECT," *IEEE Transactions on Medical Imaging*, vol. 5, pp. 61–66, June 1986.